IEEE Access
Multidisciplinary : Rapid Review : Open Access Journal

Received 31 August 2022, accepted 13 September 2022, date of publication 20 September 2022, date of current version 27 September 2022.

Digital Object Identifier 10.1109/ACCESS.2022.3208172

RESEARCH ARTICLE

Time–Domain Electromagnetic Identification Based on Rectangular Grooves

PETR KADLEC, (Member, IEEE)
Lerch Laboratory of EM Research, Department of Radio Electronics, Faculty of Electrical Engineering and Communication, Brno University of Technology, 616 00 Brno, Czech Republic

e-mail: kadlecp@vut.cz

This work was supported by the Czech Science Foundation under Grant 20-01090S.

ABSTRACT Unique identification of goods and products is an integral part of today's automated world. Conventional optical systems cannot be operated in environments of poor visibility. The radio–frequency identification systems require expensive development, production, and installation of passive tags. In this paper, we propose a system that stores the information necessary for the distinction of individual items into a set of grooves with different geometric properties. The individual items are then identified based on observing the response to the electromagnetic wave in the time domain. The proposed identification system benefits from the cooperation of a semi–analytical computational scheme based on the Cagniard–DeHoop Method of Moments and a global optimization algorithm that solves the inverse problem of grooves characterization. The proposed system is validated on several computational examples. Also, the resilience of the proposed system to the influence of the noise added to the observed response is investigated. Finally, the influence of reflected signals on the accuracy of the system is assessed.

INDEX TERMS Radiofrequency identification, inverse method, particle swarm optimization, evolutionary computation.

I. INTRODUCTION

The identification of goods and products is addressed in many industries ranging from ordinary shops, including logistics, to high–end technology laboratories. Traditional optical bar/QR code systems are reliable and make it easy to distinguish between large numbers of individual items. Nevertheless, the use of optical systems is limited to (clean) environments through which the light can propagate without serious scattering effects [1].

Radiofrequency identification (RFID) has become one of the most widely used and profit–generating wireless systems [2]. A conventional RFID system consists of an active reader device and a passive tag attached to an item that is to be identified [3]. The design, manufacturing, and attachment of the passive tag are unavoidable steps when using RFID technology.

The contemporary RFID research focuses on the following areas. The development of chipless RFID sensors offers both increased reliability and cost-effectiveness [4], [5], [6]. Development of efficient RFID readers arrangement algorithms should enhance the capacity of the identification systems [7]. The pattern reconfigurable readers increases the RFID coverage area, can be used for the on-body implementation, and indoor localization applications [8]. Authors in [9] and [10] try to integrate the RFID systems to Internet of Things applications. Another important topic is ensuring the security of the RFID systems including used hardware [11] or software protocols [12], [13].

Nevertheless, the information necessary to distinguish individual items can be stored in a set of grooves that are scratched in an attached conducting tag or directly to a conducting surface of the item. Individual items are distinguished by altering the geometrical properties of the selected number of grooves (e.g. their depths and mutual positions). Such a system would have several advantages. The set of several grooves can be scratched on the metallic surface using a very cheap technology e.g. widely available Computer Numerical Control (CNC) machining. Last but not least, it can be operated in low visibility conditions.

The associate editor coordinating the review of this manuscript and approving it for publication was Sotirios Goudos.

This work is licensed under a Creative Commons Attribution 4.0 License. For more information, see https://creativecommons.org/licenses/by/4.0/

Wakuami *et al.* [14] proposed an identification system based on the principle of magnetic sensing. In the current paper, we propose an identification system based on the same principle that distinguishes individual items based on sensing the response to an electromagnetic (EM) plane wave. According to our knowledge, no identification system uses the sensing of time-domain (TD) scattered EM fields from a set of grooves to distinguish between a set of items.

An essential part of such a system is a tool calculating the EM fields scattered by a metallic surface with rectangular grooves. Most of the computational methods are based on integral formulation and therefore apply to the time–harmonic fields only [15], [16], [17], [18], [19]. The Finite-Difference Time-Domain approach was used to solve for the EM fields scattered by grooves in [20]. The authors in [21] proposed a method to characterize the properties of a single groove on a metallic surface by the angular distribution of the scattered light generated by a set of plane waves. Authors in [22] derived a method based on Geometric/Physical Optics to analyze the terahertz–wave scattering characteristics of objects with multiple small–scale grooves having the same dimensions. A semi–analytical method to solve for the electromagnetic (EM) scattering by a 2D groove on a perfectly electric conducting (PEC) surface was fully derived in the time domain in [23]. This approach was then extended to any number of grooves in the book [24, Ch. 13.2].

Recently, we published a feasibility study [25] in which we successfully solved the inverse problem of characterization of a single groove. More specifically, the geometrical properties of a rectangular groove were retrieved from the observed voltage response using an optimization method. In this contribution, we further extend this approach - properties of two grooves are determined based on the voltage response computed by the method introduced in [24] for a groove configuration proposed by an optimization algorithm. Throughout the paper, the computational method will be called the forward solver while the optimization algorithm will be referred to as the inverse solver. A comparative study of one local and four global optimization algorithms namely the quasi–Newton Broyden–Fletcher–Goldfarb–Shanno (BFGS) algorithm [26], and Particle Swarm Optimization (PSO) [27], Differential Evolution (DE) [28], Self–organizing Migrating Algorithm (SOMA) [29], and Genetic Algorithms (GA) [30] is performed to find the most appropriate inverse solver. The limitations of the potential identification system are critically discussed based on the results of various examples. We investigate the influence of Additive White Gaussian Noise (AWGN) and the presence of echoed signals on the reliability of the identification system.

The paper is organized as follows. Section II describes the inverse problem of characterization of geometrical properties of two rectangular grooves. It is formulated as a single-objective optimization problem. Section III reviews the numerical computational tools that solve the formulated problem. Several instances of the grooves characterization problem are defined, solved, and discussed in Section IV. Finally, Section V concludes the paper with a critical discussion of the advantages and limitations of the proposed identification system.

II. PROBLEM DESCRIPTION

The problem under consideration consisting of two rectangular grooves etched in the PEC surface, denoted by $\mathcal{G}_\mathrm{A}$ and $\mathcal{G}_\mathrm{B}$, is shown in Fig. 1. Here, the position is located using the Cartesian reference frame with the origin $\mathcal{O}$ and the (standard) base $\{\mathbf{i}_x, \mathbf{i}_y, \mathbf{i}_z\}$. The centers of the pertaining apertures are located at $\{0, 0, 0\}$ and $\{x_\mathrm{B}, 0, 0\}$, respectively. The grooves are considered to have the same width w and can vary in their depths d_A and d_B, respectively. Grooves $\mathcal{G}_\mathrm{A}$ and $\mathcal{G}_\mathrm{B}$ occupy domains $\{-w/2 < x < w/2, -\infty < y < \infty, 0 < z < -d_\mathrm{A}\}$, and $\{x_\mathrm{B} - w/2 < x < x_\mathrm{B} + w/2, -\infty < y < \infty, ..0 < z < -d_\mathrm{B}\}$, respectively.

The grooves are surrounded by a linear, isotropic and loss-free medium $\mathcal{D}_0$ that is characterized by its electric permittivity ϵ and permeability μ. Both EM parameters are considered to be scalar, real-valued, and positive. Then, the EM wave propagates through $\mathcal{D}_0$ with speed $c_0 = (\epsilon\mu)^{-1/2} > 0$ and corresponding wave admittance $Y_0 = (\epsilon/\mu)^{1/2} > 0$.

The corrugated surface is illuminated by a pulsed EM plane wave that is defined by its pulse shape, $e^\mathrm{i}(t)$, and the angle of incidence, θ. The superscript $^\mathrm{i}$ stands for "incident" and t denotes the time coordinate.

The proposed identification system is supposed to distinguish individual users (or shortly IDs) based on sensing the scattered EM fields in a form of the voltage response measured over the grooves. Every ID then has its own unique set of grooves. The degrees of freedom are geometrical properties of the grooves namely depths d_A, and d_B, and their mutual distance x_B. To recognize a correct ID (i.e. values d_A, d_B, and x_B) based on the observed voltage V^o pretends an inverse problem. The inverse problem is solved using the global optimization algorithm (inverse solver), that proposes a candidate solutions whose correctness is evaluated by the CDH–MoM (forward solver) until the correct ID is not determined.

The inverse problem of determining the geometrical properties of the grooves can be formulated as a single– objective optimization problem:

$$\begin{aligned} \min_{\boldsymbol{u}} \quad & f(\boldsymbol{u}) = \sum_{k=1}^{N^\mathrm{t}} \left| V_k^\mathrm{c}(\boldsymbol{u}) - V_k^\mathrm{o} \right| \\ \text{s.t.} \quad & \boldsymbol{u} \in \Gamma \end{aligned} \tag{1}$$

where $k = 1, 2, 3, \ldots, N^\mathrm{t}$ denotes individual time samples, N^t is the total number of samples considered. Furthermore, symbol V_k stands for the k-th sample of the voltage induced across the grooves. Superscripts $^\mathrm{c}$ and $^\mathrm{o}$ distinguish the voltage being "computed" (by a forward solver) and "observed" (e.g. by measurement, or by a forward solver with an added AWGN). The decision space vector $\boldsymbol{u}$ consists of three parameters of the analyzed configuration $\{d_\mathrm{A}, d_\mathrm{B}, x_\mathrm{B}\}$. They are highlighted in red in Fig. 1. The symbol Γ denotes the decision space (all feasible combinations of d_A, d_B, and x_B).

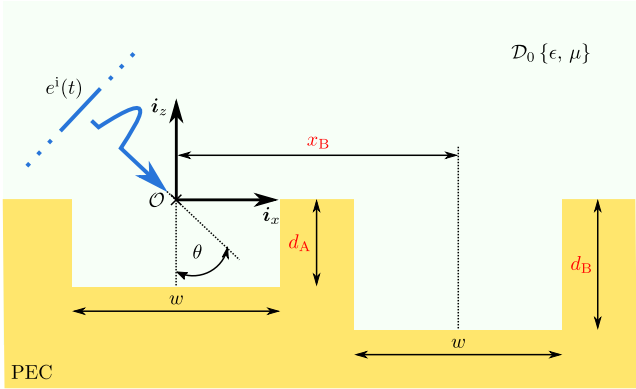

FIGURE 1. Two rectangular grooves in a PEC surface (the variables of the decision space are highlighted in red).

Objective function (1) simply minimizes the absolute error between the observed voltage and the one computed based on parameters proposed by the forward solver (optimization algorithm).

III. COMPUTATIONAL METHODS

The whole process of solving the inverse problem (see (1)) is governed by the inverse solver. Any single–objective constrained optimization algorithm can be used as the inverse solver. The inverse solver proposes estimations of the decision space variables $\boldsymbol{u} = \{d_{\mathrm{A}}, d_{\mathrm{B}}, x_{\mathrm{B}}\}$. The forward solver then computes the voltage $\boldsymbol{V}^{\mathrm{c}}$ for the particular $\boldsymbol{u}$ to evaluate it using (1) whose value indicates the quality of the proposed $\boldsymbol{u}$.

Concerning the efficiency and robustness of the solution, we opted for the PSO algorithm as the inverse solver. As shown by the results of our previous work [25] and in Fig. 6, it outperforms the other state–of–the–art algorithms BFGS, DE, SOMA, and GA significantly. The forward and inverse solvers are briefly reviewed in the following subsections.

A. FORWARD SOLVER

The full derivation of the method based on the reciprocity theorem of the time-convolution type [31] and the Cagniard–DeHoop Method of Moments (CDH–MoM) [32] can be found in [24, Ch. 13.2]. Pursuing this approach, the voltage response of the surface $\boldsymbol{V}^{\mathrm{c}}$ on the EM pulse $e^{\mathrm{i}}(t)$ can be obtained via the marching–on–in–time technique:

$$\boldsymbol{V}_m = \boldsymbol{Y}_1^{-1} \cdot \left[\boldsymbol{H}_m - \sum_{k=1}^{m-1} \left(\boldsymbol{Y}_{m-k+1} - 2\boldsymbol{Y}_{m-k} + \boldsymbol{Y}_{m-k-1}\right) \cdot \boldsymbol{V}_k\right] \quad (2)$$

for $m = 1, 2, \ldots, N^{\mathrm{t}}$ being the indexes of the time samples. Symbol $\boldsymbol{Y}_1^{-1}$ denotes the inverse of the admittance matrix for the first time step $t_1 = \Delta t$. The excitation of the system (2) is given by

$$\boldsymbol{H}_m = \begin{bmatrix} -2Y_0 e^{\mathrm{i}}(t_m) \\ 0 \end{bmatrix}, \quad (3)$$

where Y_0 is the free–space admittance. The elements of 2×2 matrices $\boldsymbol{Y}_k$ in (2) are obtained:

$$\boldsymbol{Y}_k = \frac{2Y_0}{c_0 \Delta t} \begin{bmatrix} \Phi_{\mathrm{A}}(t_k) & \Psi(t_k)/2 \\ \Psi(t_k)/2 & \Phi_{\mathrm{B}}(t_k) \end{bmatrix}, \quad (4)$$

where $\Psi(t)$ is given by

$$\Psi(t) = \frac{1}{2\pi} \cosh^{-1}\left(\frac{c_0 t}{x_{\mathrm{B}}}\right) \mathrm{H}\left(t - \frac{x_{\mathrm{B}}}{c_0}\right), \quad (5)$$

where symbol $\mathrm{H}(t)$ stands for the Heaviside unit step function. Then, the main diagonal components of (4) are given by

$$\Phi_{\mathrm{A,B}}(t) = \left[\Phi(t) + \Phi^{-}_{\mathrm{A,B}}\right]/2. \quad (6)$$

The TD function for $\Phi(t)$ reads

$$\Phi(t) = \left[\Upsilon^{\mathrm{B}}(w, t) - 2\Upsilon^{\mathrm{B}}(0, t) + \Upsilon^{\mathrm{B}}(-w, t)\right]/w^2, \quad (7)$$

where

$$\Upsilon^{\mathrm{B}}(x, t) = \frac{1}{2\pi}\left\{\frac{x^2}{2}\cosh^{-1}\left(\frac{c_0 t}{|x|}\right) + \frac{c_0 t x}{2}\left(\frac{c_0^2 t^2}{x^2} - 1\right)^{1/2} - c_0 t |x| \tan^{-1}\left[\left(\frac{c_0^2 t^2}{x^2} - 1\right)^{1/2}\right]\right\} \cdot \mathrm{H}\left(t - \frac{|x|}{c_0}\right) + \frac{c_0 t x}{2}\mathrm{H}(x)\,\mathrm{H}(t), \quad (8)$$

for all $x \in \mathbb{R}$ and $t > 0$. The limit for $x = 0$ is then

$$\Upsilon^{\mathrm{B}}(0, t) = \frac{c_0^2 t^2}{4\pi}\mathrm{H}(t). \quad (9)$$

Finally, the second component of (6) is given by

$$\Phi^{-}_{\mathrm{A,B}} = \left[\frac{c_0 t}{2w}\mathrm{H}(t) + \frac{1}{w}\sum_{n=1}^{\infty}\left(c_0 t - 2n d_{\mathrm{A,B}}\right)\mathrm{H}\left(c_0 t - 2n d_{\mathrm{A,B}}\right)\right]. \quad (10)$$

Throughout this study, we use a TD causal bipolar pulse with the triangular signature defined as [23]

$$e^{\mathrm{i}}(t) = \frac{2}{t_{\mathrm{w}}}\Big[t\mathrm{H}(t) - (2t - t_{\mathrm{w}})\mathrm{H}(2t - t_{\mathrm{w}}) + (2t - 3t_{\mathrm{w}})\mathrm{H}(2t - 3t_{\mathrm{w}}) - (t - 2t_{\mathrm{w}})\mathrm{H}(t - 2t_{\mathrm{w}})\Big] \quad (11)$$

to excite the grooves. In (11), symbol t_{w} denotes the base length of the triangle pulse. The pulses impinging grooves $\mathcal{G}_{\mathrm{A}}$ and $\mathcal{G}_{\mathrm{B}}$ are shown in Fig. 2. The delay between the time of arrivals depends on the distance of grooves x_{B} and on the incident angle θ. The pulse (11) can be easily generated on a standard signal generator [33].

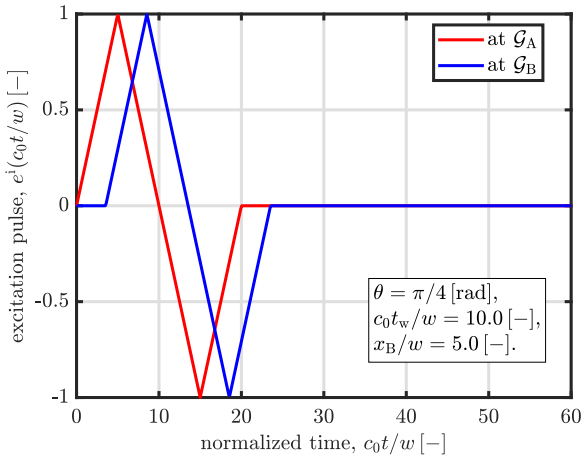

FIGURE 2. Signature of the excitation pulse $e^i(t)$ at grooves $\mathcal{G}_A$ and $\mathcal{G}_B$.

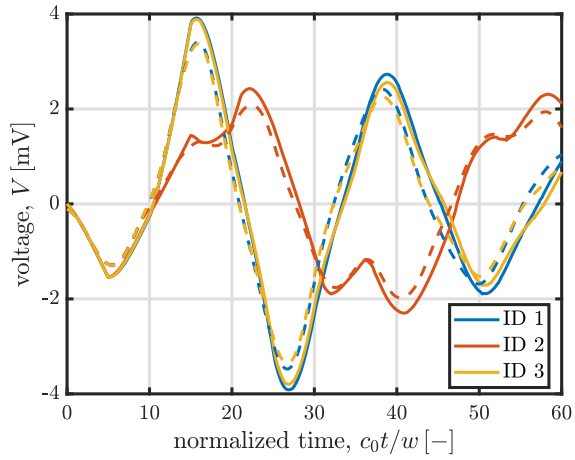

FIGURE 3. Comparison of voltage responses observed by CDH–MoM (solid curves) and CST (dashed curves) solvers for three problem instances ID 1 ($d_A/w = 5.0$, $d_B/w = 5.0$, $x_B/w = 7.0$), ID 2 ($d_A/w = 8.0$, $d_B/w = 5.0$, $x_B/w = 5.0$), and ID 3 ($d_A/w = 5.0$, $d_B/w = 5.0$, $x_B/w = 6.0$).

The accuracy of the forward solver is validated by a direct comparison with the full–wave solver CST Microwave Studio. The voltage responses obtained by the CDH–MoM and CST for three different configurations of the grooves ID 1-3 are shown in Fig. 3. Here, voltages over grooves $\mathcal{G}_A$ and $\mathcal{G}_B$ observed by both computational methods are in an excellent agreement. However, the calculation of one configuration of grooves takes only a few ms using CDH–MoM while one run of CST takes about 250 s. This difference in computation times brings a significant acceleration of the whole identification process because the forward solver is called by the inverse solver several times during the identification process.

The responses shown in Fig. 3 indicate the variation of the observed TD responses when changing grooves parameters d_A, d_B, and x_B. The responses are completely different when two of three parameters are changed like in case of ID 1 and ID 2. The responses have a similar shape if only one of the parameters is slightly changed like in case of ID 1 and ID 3. Nevertheless, as shown by the results presented below (please refer to Fig. 7) the sum of differences between those two curves provides still enough information to the PSO inverse solver to distinguish between the two IDs provided by these two configurations.

To further show that the proposed system will be able to safely distinguish between IDs, we introduce the quantity of the objective function margin:

$$\Delta = 10 \log \frac{\min\limits_{\forall \boldsymbol{u} \in \Gamma, \boldsymbol{u} \neq \mathrm{ID}} \sum\limits_{k=1}^{N^t} |V(\boldsymbol{u}) - V^{\mathrm{ID}}|}{\sum\limits_{k=1}^{N^t} |V^{\mathrm{ID}}|}, \tag{12}$$

Quantity Δ simply shows what is the difference between the observed voltage for the particular ID V^{ID} and the other ID that produces the most similar voltage response. Larger values of Δ should mean easier identification of the particular ID. A zero signal would have the margin $\Delta = 0$ dB.

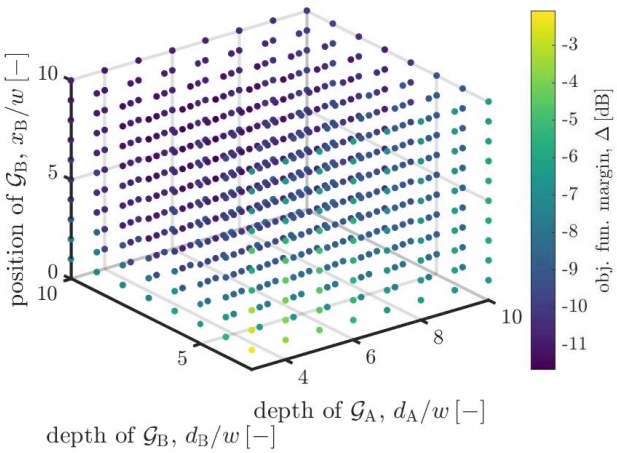

FIGURE 4. The objective function margin Δ for all possible IDs of the proposed system.

The distribution of the margin quantity over all IDs of the proposed system is shown in Fig. 4. The value of $\Delta = -10$ dB can be expected for the whole decision space Γ what should be sufficient for a reliable identification.

B. INVERSE SOLVER

Any single–objective optimization algorithm can be used as the inverse solver of problem (1). The effectiveness of the optimization process varies when using different optimizers on the same problem according to the well–known "No free lunch" theorem [34]. Therefore, we have tried different state–of–the–art optimization algorithms on the single groove characterization problem [25] and as well in the current study where we face the problem to characterize two grooves. Namely, we compare the results obtained by quasi–Newton BFGS method [26], PSO [27], DE [28], SOMA [29], and GA [30]. As shown by the results (please, refer to Sec. IV and [25, Sec. IV]), PSO outperforms the other algorithms for this

type of optimization problem. For the sake of brevity, we shall limit our description to the PSO algorithm only.

PSO was introduced by Kenedy and Eberhart [35]. It fully exploits the intelligence of the swarm of particles. By a particle, we mean a decision space vector $\boldsymbol{u}$ that moves in individual iterations of the algorithm based on information about the decision space obtained so far by the whole swarm. PSO starts with a random generation of positions $\boldsymbol{u}$ (and velocities $\boldsymbol{v}$) for individual particles:

$$\boldsymbol{u}_p = \boldsymbol{u}_{\min} + \boldsymbol{r} \odot (\boldsymbol{u}_{\max} - \boldsymbol{u}_{\min}) \tag{13}$$

Both $\boldsymbol{u}$ and $\boldsymbol{v}$ are vectors of length D which is the number of decisions space variables (i.e. optimized parameters). Index p denotes the p-th particle, $\boldsymbol{u}_{\min}$ and $\boldsymbol{u}_{\max}$ are the lower and upper limits of the decision space Γ, and $\boldsymbol{r}$ denotes the random vector of values chosen from interval $\langle 0, 1\rangle$ with a uniform probability. Symbol $\odot$ has the meaning of the element–wise multiplication of two vectors with the same lengths.

Every particle then changes its position in every iteration i according to the formula

$$\boldsymbol{u}_p(i) = \boldsymbol{u}_p(i-1) + \Delta t \boldsymbol{v}_p(i) \tag{14}$$

where Δt is the time step that equals 1 and is present for the sake of physical correctness, only.

The most important equation of the PSO algorithm is the velocity update formula that reads:

$$\begin{aligned}\boldsymbol{v}_p(i) = {} & w\boldsymbol{v}_p(i-1) + c_1 r_1 \left[\boldsymbol{pb}_p - \boldsymbol{u}_p(i-1)\right] \\ & + c_2 r_2 \left[\boldsymbol{gb} - \boldsymbol{u}_p(i-1)\right].\end{aligned} \tag{15}$$

Here, w, c_1, and c_2 are the user–defined parameters controlling the flow of the algorithm namely the inertia weight, the cognitive learning factor, and the social learning factor, respectively. Symbol r denotes the random number from interval $\langle 0, 1\rangle$, again. Finally, symbols $\boldsymbol{pb}$ and $\boldsymbol{gb}$ stand for the personal and global best position, respectively. Every particle keeps its own $\boldsymbol{pb}$ where it found so–far the best value of the objective function. Global best is then the best position visited by the whole swarm.

Equation (15) redirects the particles based on three tendencies that are balanced partially by the user's choice (values of parameters w, c_1, and c_2) and partially by the randomness (values r_1, and r_2): 1) a particle remains to move in its previous direction (controlled by w), 2) a particle is attracted to its $\boldsymbol{pb}$ position (controlled by c_1, r_1), and 3) a particle is attracted to the global best position $\boldsymbol{gb}$ (controlled by c_2, r_2). The proper setting of w, c_1, and c_2 balances the exploitation and exploration properties of the algorithm.

After the new position for each particle is set according to (14), these positions are checked if they are feasible (i.e. inside of the decision space Γ). If any of them is out of Γ, one of the absorbing, reflecting, or invisible boundary conditions has to be applied to the violating particles [36]. Then, the new positions $\boldsymbol{u}(i)$ are evaluated using the objective function f (1). The personal best positions and the global best positions are updated for the particles that find better positions. This process repeats until the stop condition is met. Usually, the maximal number of iterations I is used as one of the conditions along with the sufficient value of the objective function. The pseudocode of the PSO algorithm is summarized in Alg. 1.

Algorithm 1 Pseudocode of the PSO Algorithm

Input: Set of parameters $\mathcal{S}$, objective function f, decision space Γ
Output: Vector $\boldsymbol{u} \in \Gamma$ with $\min f(\boldsymbol{u})$

```
Generate random particles and velocities u, v ∈ Γ
Compute f(u)
while i ≤ I do
    Update v(i) and u(i)
    Check u(i) ∈ Γ
    Compute new f(u(i))
    Update pb and gb
    i = i + 1
end while
```

IV. RESULTS

We performed several experiments to assess the feasibility of the proposed methodology in the identification problem. Accordingly, the system consisting of the forward and inverse solver as described in the previous section is asked to find the geometrical properties of two grooves. The quality of the search is expressed through the decision space error [25]:

$$\mathrm{DER} = \left[\sum_{d=1}^{D}\left(u_d^{\mathrm{best}} - u_d^{*}\right)^2\right]^{1/2}, \tag{16}$$

where superscript * marks the true (optimal) decision space vector and ^{best} indicates the decision space vector found by the optimization algorithm. Symbol D is the size of the decision space ($D = 3$ for our problem). The DER value is simply the Euclidean distance between the found and correct solutions. It should be noted that DER is normalized with respect to the grooves' width. We take $w = 1.0$ mm in the examples that follow.

All the tests were performed 100–times to eliminate statistical anomalies that can occur when using stochastic optimization algorithms such as PSO. All the tests are carried out for the decision space Γ defined as follows: $\{3.0 < d_{\mathrm{A}}/w < 10.0\}$, $\{3.0 < d_{\mathrm{B}}/w < 10.0\}$, and $\{1.0 < x_{\mathrm{B}}/w < 10.0\}$. The limits of the proposed Γ are selected taking into account the capabilities of today's signal generators [33, Ch. 5] and the spatial possibilities - the grooves used for the identification should not occupy an exceedingly large area or/and be too deep.

The parameters of the excitation pulse are presented in Fig. 2. The voltage responses used to compute objective function (1) have $N^{\mathrm{t}} = 101$ samples. A single run of the forward solver takes approximately 4.0 ms on a standard PC. The optimization algorithms implemented in FOPS (an in–house MATLAB toolbox [36]) were used. All the

tests could use 1000 objective function evaluations during one run (i.e. 20 agents and 50 iterations). Default values of controlling parameters as defined in FOPS were used for individual optimizers (please refer to [36] for further details).

The objective function of a problem instance having $d_A^*/w = 5.0$, $d_B^*/w = 7.0$, and $x_B^*/w = 5.0$ is shown in Fig. 5. There, three cuts are shown to better visualize the 3D function ($x_B = x_B^*$ for the d_A-d_B cut and so forth). It can be seen, that the objective function is relatively smooth and valley–shaped for all three cuts. The objective function value increases most rapidly with a change of the d_A value. But the most important finding is that the objective function has a distinguishable difference between the f value for the optimal $\boldsymbol{u}^*$ and for $\boldsymbol{u}$ in a close distance from $\boldsymbol{u}^*$. Let us consider the distance $1 \times w$ as a close one. This distance is crucial for the intended identification system.

A. COMPARATIVE STUDY

The effectiveness of the optimization algorithm as an inverse solver is the most important parameter for the potential identification system. Too slow convergence or a large variation in the results would disqualify the system to be used for real–life applications. Therefore, we assessed five algorithms to see which one converges most quickly and surely to the global optimum. Namely, we compared BFGS, PSO, DE, SOMA, and GA algorithms.

Results of the DER metric for individual algorithms are summarized in the form of standard boxplots in Fig. 6. The BFGS algorithm achieved the worst results which is not surprising as it was started at the random position in Γ for every run. Quasi–Newton methods tend to converge to the closest local optimum. PSO outperforms also the other global algorithms (DE, SOMA, GA). The worst results obtained by PSO are at the same level of DER as the best results of the other algorithms. The median value obtained by PSO is approximately two orders of magnitude better than the median values of DE, SOMA, and GA. The excellent results of PSO are caused by the valley–shaped nature of the objective function and the low number of decision space variables $D = 3$. Usually, DE and GA outperforms PSO in case of higher dimensions $D \gg 10$ [37].

In this study, we consider an identification system with individual items characterized by three geometrical properties d_A, d_B, and x_B. Individual users are mutually differentiated by changing one of the three parameters by at least $1 \times w$. Therefore, the critical value of the DER metric meaning that the inverse solver was successful or not is DER $= 0.5$ (it is shown as a red dashed line in Fig. 6). Only PSO and DE achieved DER well below this particular value for all independent runs which means that these two algorithms were successful in all runs. Using PSO, there is still a margin of two orders in magnitude. Therefore, a lower number of agents and iterations could be used to make the identification process faster.

B. RELIABILITY

Another watched parameter of every system is its reliability. Thanks to the fact, that our identification system has only three degrees of freedom, we tested the PSO inverse solver for all the possible combinations that are feasible according to Γ (see Sec. IV). Considering that all the parameters are sampled with $1 \times w$ our system can distinguish $8 \times 8 \times 10$ users. All the resulting 640 problem instances were solved 100 times by the PSO inverse solver. The mean value of DER metric is plotted as a sliced 3D graph in Fig. 7.

We can see the shades of dark blue colors in the whole range of 3D space Γ. The DER grows to larger values only for the lower limit of $\mathcal{G}_A$ depth $d_A/w = 3.0$. These errors are caused by the numerical issues of the forward solver. The numerical discrepancies can be neglected by reducing the width of the spatial support of the excitation pulse or by decreasing the time step Δt. The first option may run into the limits of available signal generators. The second option will lead to a slowdown of the identification process. Nevertheless, the capacity of the identification system can be enhanced by adding more grooves which requires only a minor change in the forward solver.

C. RESILIENCE TO NOISE

In a real scenario, the influence of noise corrupting the "observed" signal $\boldsymbol{V}^o$ has to be taken into account. Therefore, the response $\boldsymbol{V}^o$ was corrupted by the additive white Gaussian noise. AWGN with SNR $= \{5.0, 10.0, 15.0, 20.0, 25.0, 30.0\}$ (in dB) was added to $\boldsymbol{V}^o$. The statistical results are shown in Fig. 8. Here, we can observe that the proposed system can identify the correct user in 100% of cases for SNR ≥ 15.0 dB. Only a few outliers (5 of 100 trials) are misidentified for SNR $= 10.0$ dB.

D. ECHO SIGNAL INFLUENCE

In this experiment, we analyze the impact of a delayed and attenuated signal (e.g. a reflected signal) on the accuracy of identification. For these purpose, the observed signal $\boldsymbol{V}^o$ is composed of two voltages: the primary response $\boldsymbol{V}_p$ (with no delay or attenuation) and echoed response $\boldsymbol{V}_e$. The echoed voltage is attenuated 10-times and is delayed by a value τ. An example of the thus distorted voltage signal is shown in Fig. 9.

The DER values for different values of the delay $\tau c_0/w = \{5.0, 10.0, 20.0, 50.0\}$ are shown in Fig. 10. The influence of the echoed signal increases with the decreasing delay τ when the echo signal changes the strong initial part of the observed pulse. On the contrary, the observed voltage is corrupted by zeros for the most time samples when τ becomes large in comparison to spatial parameters of grooves. Fig. 10 shows that the identification is virtually flawless for $\tau c_0/w \geq 10$. Therefore, the proposed approach can easily handle unwanted signals due to scattering by objects located in the close vicinity of the device under test.

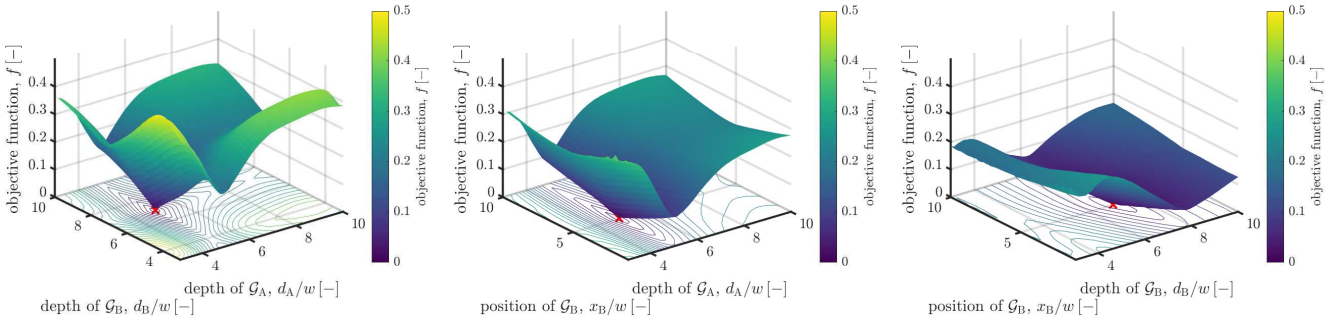

(a) $x_\mathrm{B}/w = x_\mathrm{B}^*/w = 5.0$ (b) $d_\mathrm{B}/w = d_\mathrm{B}^*/w = 7.0$ (c) $d_\mathrm{A}/w = d_\mathrm{A}^*/w = 5.0$

FIGURE 5. Three cuts of the objective function for problem instance: $d_\mathrm{A}^*/w = 5.0$, $d_\mathrm{B}^*/w = 7.0$, and $x_\mathrm{B}^*/w = 5.0$.

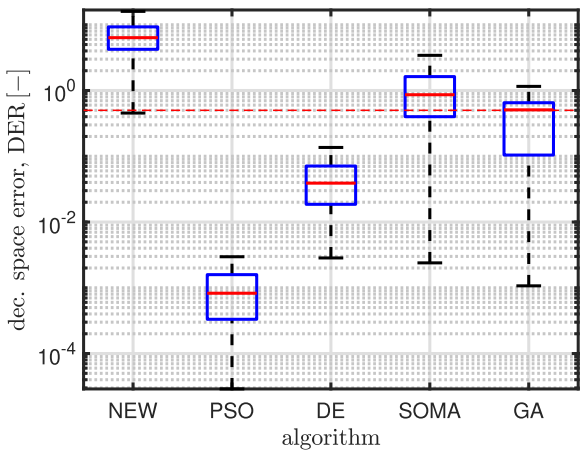

FIGURE 6. Achieved decision space error DER for different optimization algorithms.

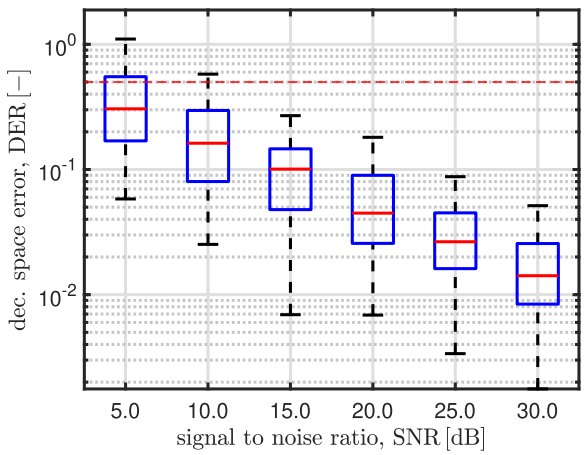

FIGURE 8. Decision space error DER for PSO algorithm for various SNR values of noise added to the "observed" signal.

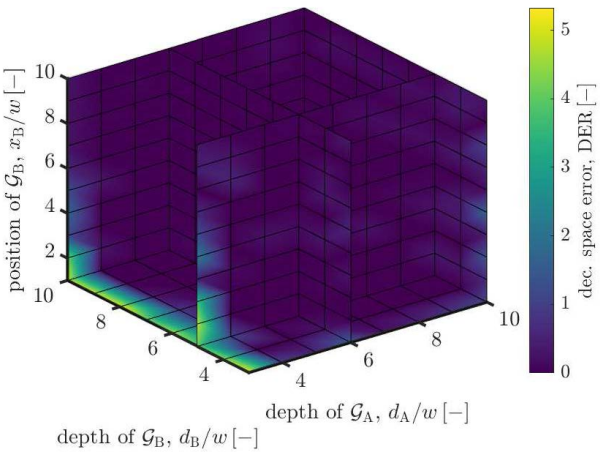

FIGURE 7. Decision space error DER for PSO algorithm for all possible instances of problem (1) when individual parameters d_A, d_B, and x_B are sampled with step $1 \times w$.

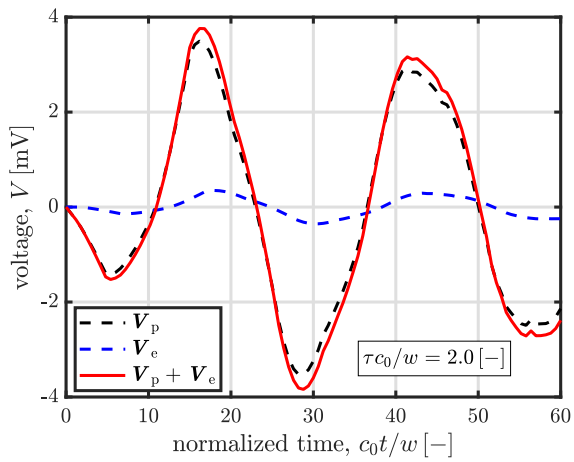

FIGURE 9. The observed signal V^O when it is composed of a primary signal V_p and an echoed signal V_e with normalized parameter $\tau c_0/w = 2.0$.

E. SENSOR POSITION INFLUENCE

In the current state, the TD response V is observed just above the aperture of the grooves. The real-life system would need a sensor to be placed at a certain distance from the screen. As the reflected field above the analyzed structure can be attributed to the voltage response (that equals to the

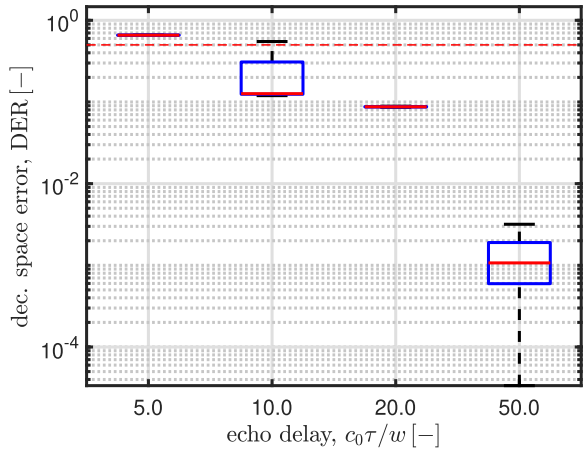

FIGURE 10. The observed DER values for different delay τ of the echoed signal V_e.

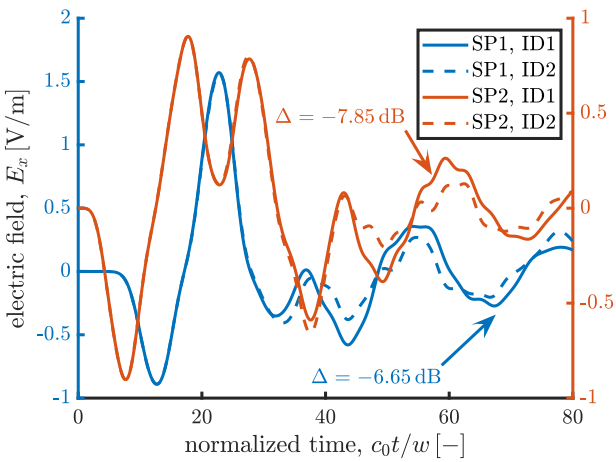

FIGURE 11. The electric field TD pulses observed at SP1 ($x_S/w = 10.0$, $y_S/w = 20.0$), and SP2 ($x_S/w = 50.0$, $y_S/w = 50.0$) for ID1 (solid curves) and ID2 (dashed curves). Data computed by CST Microwave Studio.

equivalent magnetic-current surface density) it could be evaluated through a space-time convolution with the pertaining 2-D Green's function [31]. This continuation of the voltage response to the upper space will then, indeed, change both the amplitude and shape of the TD response. Nevertheless, the same effect on the observed pulse can also be achieved by changing the properties of the initial pulse $e^{\mathrm{i}}(t)$.

The effect of the sensor lateral position x_S and height y_S above the screen on the observed response is shown in Fig. 11. Here, the electric field TD pulses observed at two different positions of the sensor (SP1, SP2) for two different IDs (ID1, ID2, see Fig. 3) are compared. The TD pulses were obtained using the CST Microwave Studio. Especially the later parts of the pulses are well distinguishable for the same SP and different ID. The objective function margin between the two IDs Δ is well below -10 dB for both locations ($\Delta = -6.95$ dB for SP1, and $\Delta = -7.85$ dB for SP2). As shown by the results presented earlier, this value of Δ is sufficient for the optimization algorithms to securely identify the correct ID.

V. CONCLUSION

This paper proposes the identification system based on a solution to the grooves characterization problem. The individual items are distinguished by a unique set of grooves etched on their surface or an attached conducting tag. The grooves have different depths and mutual positions. The characterization problem is solved by employing two powerful computational tools: a semi–analytical scheme based on the Cagniard–DeHoop method of moments is used as the forward solver and a stochastic optimization technique is used as the inverse solver. Results of the comparative study show that PSO is the most efficient optimization algorithm from the chosen set of tested algorithms. Furthermore, we demonstrated that the proposed identification approach works well in the presence of noise signals.

The proposed system has several advantages compared to traditional optical or RFID systems. There is no need to design passive tags or bar codes. The grooves can be etched by a widely–available CNC technology directly into the conducting surface. The system can be operated even in places with poor visibility. Next, the number of distinguishable items grows exponentially with the number of used grooves. The results show, that 640 items can be easily distinguished using only two grooves with spatial step 1 mm. On the other hand, the number of grooves cannot grow to infinity because the accuracy of the optimization algorithm would decrease thanks to the curse of dimensionality. Also, the dimensions of the grooves have to be selected with regard to the capabilities of available signal generators.

ACKNOWLEDGMENT

The author would like to thank Dr. Martin Štumpf for providing the code serving as the forward solver, for valuable discussions of the problem, and proofreading of this manuscript.

REFERENCES

[1] M. Zhou, Q. Wang, T. Lei, Z. Wang, and K. Ren, "Enabling online robust barcode-based visible light communication with realtime feedback," *IEEE Trans. Wireless Commun.*, vol. 17, no. 12, pp. 8063–8076, Dec. 2018.

[2] A. Lozano-Nieto, *RFID Design Fundamentals and Applications*. Boca Raton, FL, USA: CRC Press, 2017.

[3] A. Haibi, K. Oufaska, K. E. Yassini, M. Boulmalf, and M. Bouya, "Systematic mapping study on RFID technology," *IEEE Access*, vol. 10, pp. 6363–6380, 2022.

[4] L. Shahid, H. Shahid, M. A. Riaz, S. I. Naqvi, M. J. Khan, M. S. Khan, Y. Amin, and J. Loo, "Chipless RFID tag for touch event sensing and localization," *IEEE Access*, vol. 8, pp. 502–513, 2020.

[5] P. Fathi, N. C. Karmakar, M. Bhattacharya, and S. Bhattacharya, "Potential chipless RFID sensors for food packaging applications: A review," *IEEE Sensors J.*, vol. 20, no. 17, pp. 9618–9636, Sep. 2020.

[6] A. Subrahmannian and S. K. Behera, "Chipless RFID: A unique technology for mankind," *IEEE J. Radio Freq. Identificat.*, vol. 6, pp. 151–163, 2022.

[7] P. Yan, S. Choudhury, and R. Wei, "A machine learning auxiliary approach for the distributed dense RFID readers arrangement algorithm," *IEEE Access*, vol. 8, pp. 42270–42284, 2020.

[8] M. A. S. Tajin and K. R. Dandekar, "Pattern reconfigurable UHF RFID reader antenna array," *IEEE Access*, vol. 8, pp. 187365–187372, 2020.

[9] A. Ghasempour, "Internet of Things in smart grid: Architecture, applications, services, key technologies, and challenges," *Inventions*, vol. 4, no. 1, p. 22, Mar. 2019.

[10] G. Zhang, S. Tao, W. Xiao, Q. Cai, W. Gao, J. Jia, and J. Wen, "A fast and universal RFID tag anti-collision algorithm for the Internet of Things," *IEEE Access*, vol. 7, pp. 92365–92377, 2019.

[11] A. Rivadeneyra, A. Albrecht, F. Moreno-Cruz, D. P. Morales, M. Becherer, and J. F. Salmeron, "Screen printed security-button for radio frequency identification tags," *IEEE Access*, vol. 8, pp. 49224–49228, 2020.

[12] L. Gao, L. Zhang, F. Lin, and M. Ma, "Secure RFID authentication schemes based on security analysis and improvements of the USI protocol," *IEEE Access*, vol. 7, pp. 8376–8384, 2019.

[13] F. Zhu, "SecMAP: A secure RFID mutual authentication protocol for healthcare systems," *IEEE Access*, vol. 8, pp. 192192–192205, 2020.

[14] H. Wakaumi, T. Komaoka, and E. Hankui, "Grooved bar-code recognition system with tape-automated-bonding head detection scanner," *IEEE Trans. Magn.*, vol. 36, no. 1, pp. 366–370, Jan. 2000.

[15] K. Barkeshli and J. L. Volakis, "Scattering from narrow rectangular filled grooves," *IEEE Trans. Antennas Propag.*, vol. 39, no. 6, pp. 804–810, Jun. 1991.

[16] D. D. Reuster and G. A. Thiele, "A field iterative method for computing the scattered electric fields at the apertures of large perfectly conducting cavities," *IEEE Trans. Antennas Propag.*, vol. 43, no. 3, pp. 286–290, Mar. 1995.

[17] Y. Shifman and Y. Leviatan, "Scattering by a groove in a conducting plane–A PO-MoM hybrid formulation and wavelet analysis," *IEEE Trans. Antennas Propag.*, vol. 49, pp. 1807–1811, 2001.

[18] E. Howe and A. Wood, "TE solutions of an integral equations method for electromagnetic scattering from a 2D cavity," *IEEE Antennas Wireless Propag. Lett.*, vol. 2, pp. 93–96, 2003.

[19] M. Bozorgi, "A generalized method for scattering from wide cavities with specified wave functions," *IET Microw., Antennas Propag.*, vol. 15, no. 1, pp. 69–79, Jan. 2021.

[20] A. Kumar Agrawal, A. Ninawe, and A. Dhawan, "Non-uniform narrow groove plasmonic nano-gratings for SPR sensing and imaging," *IEEE Access*, vol. 9, pp. 10136–10152, 2021.

[21] Z. Cao, F. Cui, F. Xian, S. Pei, J. Li, and H. Ye, "Toward characterization of a rectangular groove on a metallic surface by multi-angle light scattering," *IEEE Access*, vol. 8, pp. 60210–60217, 2020.

[22] X. Meng, L. X. Guo, C. L. Dong, and Y. C. Jiao, "GO/PO method for the terahertz scattering computation of objects with multiple small-scale grooves," *IEEE Access*, vol. 7, pp. 40738–40745, 2019.

[23] M. Štumpf, "Time-domain electromagnetic scattering by a two-dimensional narrow groove—A solution based on the Cagniard–DeHoop method of moments," *IEEE Antennas Wireless Propag. Lett.*, vol. 21, no. 3, pp. 586–589, Mar. 2022.

[24] M. Štumpf, *Metasurface Electromagnetics: The Cagniard-DeHoop Time-Domain Approach* (Electromagnetic Waves). Rijeka, Croatia: SciTech, 2022.

[25] P. Kadlec, M. Štumpf, and T. Doležal, "Towards time-domain characterization of a rectangular groove," in *Proc. Int. Symp. (ELMAR)*, 2022, pp. 1–4.

[26] R. Fletcher, *Practical Methods of Optimization*. Hoboken, NJ, USA: Wiley, 2013.

[27] J. Robinson and Y. Rahmat-Samii, "Particle swarm optimization in electromagnetics," *IEEE Trans. Antennas Propag.*, vol. 52, no. 2, pp. 397–407, Feb. 2004.

[28] K. Price, R. M. Storn, and J. A. Lampinen, *Differential Evolution: A Practical Approach to Global Optimization*. Berlin, Germany: Springer, 2006.

[29] P. Kadlec and Z. Raida, "Self-organizing migrating algorithm for optimization with general number of objectives," in *Proc. 22nd Int. Conf. Radioelektronika*, 2012, pp. 1–5.

[30] O. Cosma, P. C. Pop, and I. Zelina, "An effective genetic algorithm for solving the clustered shortest-path tree problem," *IEEE Access*, vol. 9, pp. 15570–15591, 2021.

[31] T. Adrianus and D. Hoop, *Handbook of Radiation and Scattering of Waves*. New York, NY, USA: Academic, 1995.

[32] M. Štumpf, *Time-Domain Electromagnetic Reciprocity in Antenna Modeling*. Hoboken, NJ, USA: Wiley, 2020.

[33] I. Oppermann, M. Hämäläinen, and J. Iinatti, *UWB: Theory and Applications*. Hoboken, NJ, USA: Wiley, 2004.

[34] D. H. Wolper and W. G. Macready, "No free lunch theorems for optimization," *IEEE Trans. Evol. Comput.*, vol. 1, no. 1, pp. 67–82, Apr. 1997.

[35] J. Kennedy and R. Eberhart, "Particle swarm optimization," in *Proc. IEEE ICNN*, vol. 4. Nov./Dec. 1995, pp. 1942–1948.

[36] M. Marek, P. Kadlec, and M. Čapek, "FOPS: A new framework for the optimization with variable number of dimensions," *Int. J. RF Microw. Comput.-Aided Eng.*, vol. 30, no. 9, Sep. 2020, Art. no. e22335.

[37] M. Marek and P. Kadlec, "Another evolution of generalized differential evolution: Variable number of dimensions," *Eng. Optim.*, vol. 54, no. 1, pp. 61–80, Jan. 2022.

PETR KADLEC (Member, IEEE) received the B.Sc., M.Sc., and Ph.D. degrees in electrical engineering from the Brno University of Technology (BUT), Brno, Czech Republic, in 2007, 2009, and 2012, respectively. He is currently a Researcher with the Lerch Laboratory of EM Research, Department of Radio Electronics, BUT. He has coauthored several computational toolboxes, including the Antenna Toolbox for MATLAB (AToM), and the Fast Optimization ProcedureS (FOPS). His research interests include global optimization methods and computational methods in electromagnetics.